

## ORIGINAL ARTICLE

# Direct Visualization and Mapping of the Spatial Course of Fiber Tracts at Microscopic Resolution in the Human Hippocampus

Michael M. Zeineh<sup>1</sup>, Nicola Palomero-Gallagher<sup>2</sup>, Markus Axer<sup>2</sup>, David Gräbel<sup>2</sup>, Maged Goubran<sup>1</sup>, Andreas Wree<sup>3</sup>, Roger Woods<sup>4</sup>, Katrin Amunts<sup>2,5</sup> and Karl Zilles<sup>2,6,7</sup>

<sup>1</sup>Department of Radiology, Stanford University, Lucas Center for Imaging, Stanford, CA 94305, USA, <sup>2</sup>Institute of Neuroscience and Medicine (INM-1), Research Centre Jülich, Jülich, Germany, <sup>3</sup>Institute of Anatomy, University of Rostock, Rostock, Germany, <sup>4</sup>Ahmanson-Lovelace Brain Mapping Center, David Geffen School of Medicine UCLA, Los Angeles, USA, <sup>5</sup>C. and O. Vogt Institute for Brain Research, Heinrich Heine University Düsseldorf, Düsseldorf, Germany, <sup>6</sup>Department of Psychiatry, Psychotherapy and Psychosomatics, RWTH Aachen University, Aachen, Germany and <sup>7</sup>JARA Jülich-Aachen Research Alliance, Translational Brain Medicine, Jülich, Germany

Address correspondence to Michael Zeineh, PhD, Department of Radiology, Stanford University, Lucas Center for Imaging, Rm P271, 1201 Welch Road, Stanford, CA 94305-5488, USA. Email: mzeineh@stanford.edu

## Abstract

While hippocampal connectivity is essential to normal memory function, our knowledge of human hippocampal circuitry is largely inferred from animal studies. Using polarized light microscopy at 1.3  $\mu\text{m}$  resolution, we have directly visualized the 3D course of key medial temporal pathways in 3 ex vivo human hemispheres and 2 ex vivo vervet monkey hemispheres. The multiple components of the perforant path system were clearly identified: Superficial sheets of fibers emanating from the entorhinal cortex project to the presubiculum and parasubiculum, intermixed transverse and longitudinal angular bundle fibers perforate the subiculum and then project to the cornu ammonis (CA) fields and dentate molecular layer, and a significant alvear component runs from the angular bundle to the CA fields. From the hilus, mossy fibers localize to regions of high kainate receptor density, and the endfolial pathway, mostly investigated in humans, merges with the Schaffer collaterals. This work defines human hippocampal pathways underlying mnemonic function at an unprecedented resolution.

**Key words:** entorhinal cortex, hippocampus, human circuitry, perforant pathway, polarized light microscopy

## Introduction

The medial temporal lobe (MTL) is critical to the creation, retrieval, and consolidation of new memories (Andersen 2007). Dynamic connections between its multiple components and with other parts of the brain underlie many mnemonic processes (Zeineh et al. 2003). Dysfunction of MTL components and/or

connections may explain symptoms of neurodegenerative disorders such as Alzheimer's disease (Mueller and Weiner 2009; Kerchner et al. 2012). However, circuitry of the MTL, like the rest of the human brain, is known mostly from inference based on tracer studies in animals such as rats and monkeys (Saunders and Rosene 1988; Witter and Amaral 1991; Suzuki and Amaral 1994; Chrobak and Amaral 2007; Kondo et al. 2009;

Fig. 1). Descriptions up until now of the human hippocampus have shown a different anatomy from that of other mammals both macroscopically [in primates, the dentate gyrus is dorsal to the cornu ammonis field 1 (CA1), whereas the opposite is true in rodents (Insausti and Amaral 2004)] and possibly microscopically [a white matter tract called the endfolial pathway has only been described in the human literature; (Lim, Mufson, et al. 1997)]. Detecting the structural alterations that explain

mnemonic dysfunction in hippocampal disorders requires an accurate map of the circuitry in humans. For example, the perforant path system, the connections between the entorhinal cortex (ERC) and the hippocampus, is thought to be the first white matter pathway to degenerate in Alzheimer's disease (Gómez-Isla et al. 1996), but incomplete mapping of this set of tracts has impeded efforts at direct disease detection (Kalus et al. 2006). A "ground truth", that is, the direct visualization of the nerve fibers

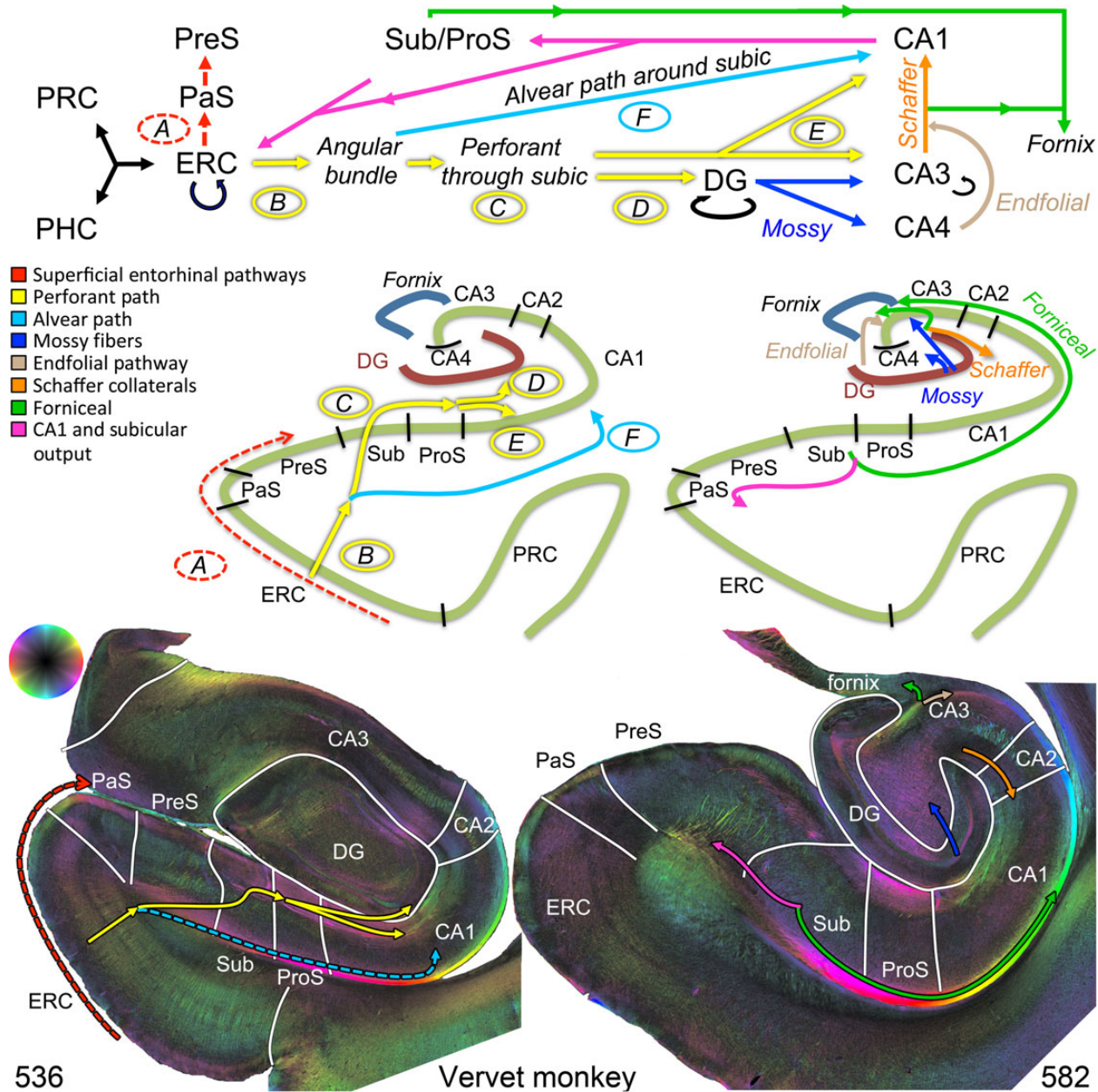


**Figure 1.** Hippocampal circuitry and validation in the vervet monkey. Top: A-F indicate the components of the perforant path system largely identified from animal studies. Major pathways are represented by solid lines, whereas minor pathways are represented by dotted lines. A = "sublamina supratangentialis" (dotted red), a minor superficial entorhinal bundle projecting to the parasubiculum and presubiculum. B = entorhinal projection to the angular bundle fibers (yellow) perforating through the subiculum. C = angular bundle fibers (yellow) perforating through the subiculum. D + E = these same fibers projecting superiorly (D) into the dentate gyrus or inferiorly (E) into the hippocampal CA fields (yellow). F = angular bundle fibers subjacent to the subiculum projecting into the CA fields (alvear path, light blue; note, for the human diagram, this pathway is larger in humans and is depicted as solid, whereas it is smaller in monkeys and depicted as dotted light blue on the bottom left). The remaining hippocampal circuitry includes: mossy fibers projecting from the dentate gyrus to CA3 and CA4 (dark blue), the endfolial pathway projecting from CA4 toward CA3 (light brown), CA3 projecting to the fornix (green) and to CA1 (Schaffer collaterals, orange), followed by CA1 and subiculum output to ERC (pink), and subicular output to the fornix (green). CA, cornu ammonis; DG, dentate gyrus; ERC, entorhinal cortex; PaS, parasubiculum; PHC, parahippocampal cortex; PRC, perirhinal cortex; PreS, presubiculum; ProS, prosubiculum; Sub, subiculum. Bottom: Polarized light microscopic images from the vervet monkey illustrate the above pathways.

building this and other pathways in the MTL, will guide efforts at noninvasive in vivo neuroimaging as well as modeling of mnemonic processes and dysfunction.

The extensive animal and limited human brain literature suggests that the perforant path system consists of the following components [Fig. 1, solid lines are prominent pathways and dotted lines are minor pathways (Witter and Amaral 1991)]:

- (A) A superficial entorhinal projection called the “sublamina supratangentialis”: This minor bundle runs in entorhinal cortical layer I along the surface of the parahippocampal gyrus toward the molecular layer of the parasubiculum and presubiculum. (Braak 1980; Insausti et al. 1995).
- (B) For the remainder of the elements of the perforant path system, the ERC projects into the angular bundle (white matter of the parahippocampal gyrus).
- (C) From the angular bundle, many fibers perforate through the subicular pyramidal layer.
- (D) A major component of these perforant fibers projects superiorly into the dentate gyrus.
- (E) The other major component of these perforant fibers projects inferiorly into the hippocampal CA fields.
- (F) Some of the angular bundle fibers remain deep to the subiculum, curve around the hippocampus within the alveus, and then turn sharply to project to CA1.

The subsequent step in the circuitry is the mossy fiber projection from the dentate gyrus to CA3 and CA4 in the hilus (Rosene and Van Hoesen 1977, 1987; Lim, Blume, et al. 1997; Kondo et al. 2008). Previously only demonstrated in humans, there is a pathway projecting downstream from CA4 known as the endfolial pathway (Lim, Mufson, et al. 1997; Parekh et al. 2015). CA3 sends output both to the fornix (Saunders and Aggleton 2007) and to CA1 via the Schaffer collaterals (Kondo et al. 2009). CA1 and the subiculum together provide output back to the ERC, with the subiculum providing additional output to the fornix (Saunders and Rosene 1988; Saunders and Aggleton 2007).

Polarized light imaging (PLI) offers direct visualization of white matter pathways without the need of any staining procedures because myelin exhibits a strong birefringence. It enables the definition of the 3D orientation of myelinated fibers at an in-plane resolution of 1.3  $\mu\text{m}$  (Axer, Amunts, et al. 2011; Axer, Gräßel, et al. 2011). This unprecedented resolving power of the trajectory of myelinated axons enables the mapping of fiber tracts in a very large brain region (see Supplementary Figs 1 and 2). In this study, we utilized PLI to identify multiple fiber tracts in the parahippocampal gyrus and the hippocampus, including the perforant path system, endfolial pathway, Schaffer collaterals, and subicular and CA1 fibers, in human and vervet monkey ex vivo tissue specimens.

## Materials and Methods

### Brain Tissue

We examined 3 human hemispheres for PLI obtained through the body donor program of the University of Rostock, Germany, in accordance with the local ethics committee. Postmortem delay was between 24 and 26 h. Two of the hemispheres were obtained from a 64-year-old male (brain #1) who died of pancreatic cancer and subsequent biliary obstruction. The patient had diabetes for 8 years and cardiomyopathy for 10 years. One left hemisphere came from a 79-year-old female who died of cardiac failure and suffered from diabetes type 2 and essential hypertension (brain #2). We also examined both hemispheres of an adult male vervet

monkey (age 2.5 years) that were perfusion fixed in accordance with the UCLA Chancellor's Animal Research Committee (ARC) ARC #2011-135 and by the Wake Forest Institutional Animal Care and Use Committee IACUC #A11-219.

Kainate receptors were visualized by means of in vitro receptor autoradiography in 5 female brains (age range 65–89) obtained through the body donor program of the University Düsseldorf, Germany, in accordance with the local ethics committee. Causes of death were cardiac arrest, pneumonia, pancreas carcinoma, or gastric bleeding. Postmortem delay was between 8.3 and 16 h. None of the patients had a history of neurological or psychiatric diseases.

### Preparation of Brains for Polarized Light Imaging (PLI)

Human brains were removed from the skull, and fixed in 4% formalin. Both hemispheres were separated. The vervet monkey was deeply anaesthetized with ketamine–pentobarbital and its brain perfusion fixed with a 4% paraformaldehyde solution. After cryoprotection with 20% glycerin, all tissue blocks were frozen. Two left human hemispheres and the vervet monkey brain were sectioned coronally, and the right human hemisphere sagittally, all at 70- $\mu\text{m}$  thickness using a large-scale cryostat microtome (Polaron CM 3500, Leica, Germany). During sectioning, each blockface of the frozen tissue was digitized with a CCD camera to obtain an undistorted reference image. These blockface images were serially aligned by means of rigid registration of the fiducial marker system ARTag mounted underneath the frozen block of tissue (Fiala 2005; Wagner and Schmalstieg 2007). ARTag markers are bitonal planar patterns, containing a unique ID number encoded with robust digital techniques of checksums and forward error correction, which was useful for automated detection and alignment across images. This registration produced volumetric images of each frozen human hemisphere (Fig. 2A–D) and for the vervet monkey brain.

### Image Acquisition and Processing

The sections were mounted on glass slides with 20% glycerin and coverslipped. Each section was imaged at 18 equidistant rotation angles of a polarimeter covering an angle range between 0° and 170°. The PLI raw images were acquired on a Taorad LMP-1 microscope with 2.7  $\times$  2.7 mm<sup>2</sup> overlapping tiles at an image size of 2400  $\times$  2400 pixel. The image pixel size was 1.3  $\times$  1.3  $\mu\text{m}^2$  in-plane. The optical resolution was approximately 3  $\mu\text{m}$ . Beforehand, a calibration scan was obtained on a blank slide and used for shading correction. Images were stitched using scale-invariant feature transform landmarks in the overlapping zones. The individual rotational images were fit to a three-parameter model based on a Fourier series solution to the Jones calculus to create maps of fiber orientation, inclination, and transmittance (Axer, Gräßel, et al. 2011). Transmittance images were normalized by dynamic range. Coregistered color fiber orientation maps were weighted by the normalized transmittance images and depicted in-plane fiber orientation according to color (see Supplementary Fig. 1, color wheels in Figs 1 and 3–7) and inclination according to darkness (darker means more through-plane orientation, at the center of the color wheel).

The PLI process produces fiber orientation (Fig. 1, bottom row) and transmittance images (Figs 2E–G and 3B). The transmittance images resemble a “hybrid stain” combining the appearance of both cell body and myelin-stained sections in the same image because of the low transmittance properties of cell bodies and myelin. Since transmittance and fiber orientation images are acquired from identical sections, they are automatically coregistered and can easily be compared. The transmittance images

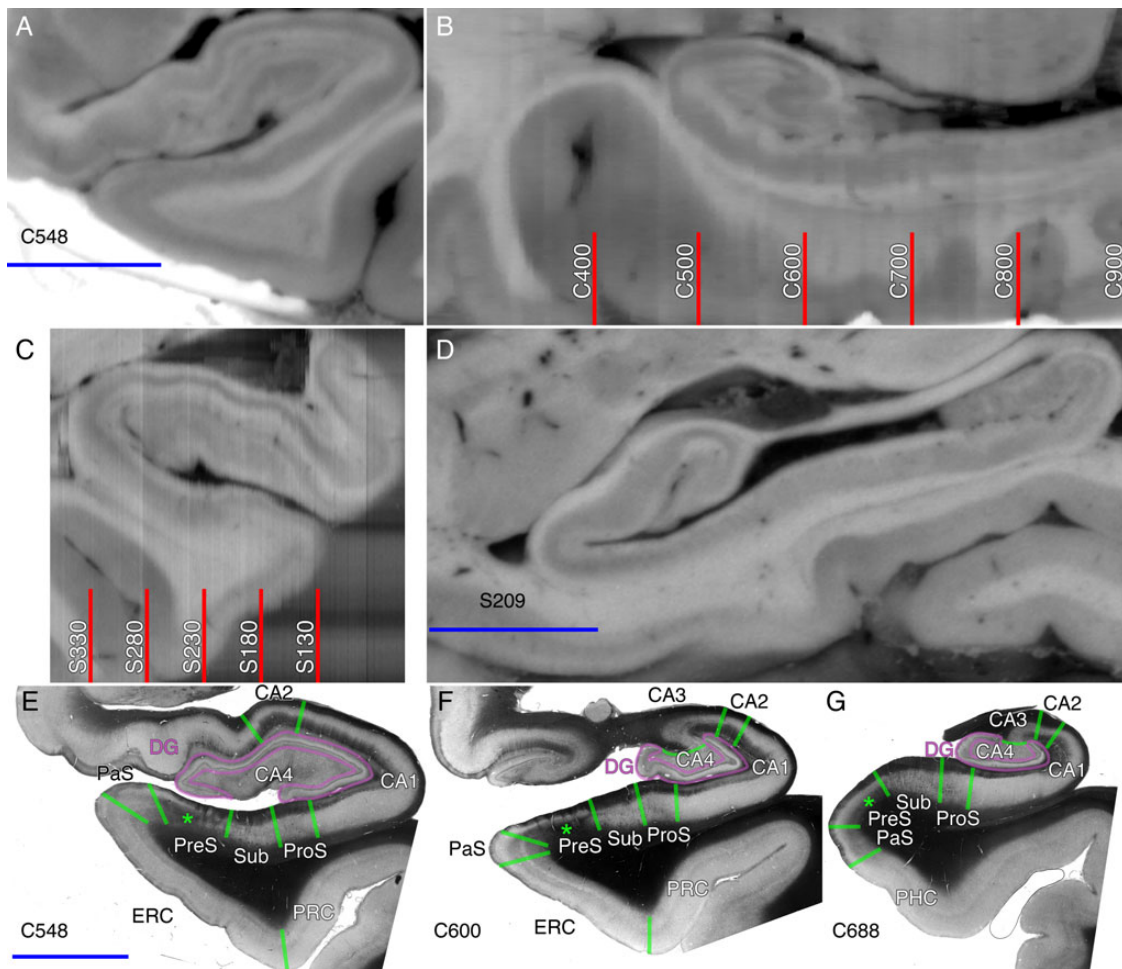


**Figure 2.** Sectioning and segmentation procedure from the left (A,B) and right (C,D) hemispheres of brain #1. (A) Example coronal blockface image from the left hemisphere from brain #1, section 548. (B) Sagittal reformat of coregistered serial coronal blockface sections with the numbers indicating the coronal slice number. (C) Coronal reformat of coregistered serial sagittal blockface sections from the right hemisphere from brain #1, with the numbers indicating the sagittal slice number. (D) Sagittal blockface image from the right hemisphere, slice 209. (E–G) Coronal transmittance images with overlaid medial temporal subregion demarcations in green. For the remainder of the figures, subregion demarcations will also be in green. The green asterisks highlight the darkening associated with myelin in the deep presubicular pyramidal cell layer that facilitates its segmentation. The blue scale bar is 1 cm in length.

were used to segment the hippocampal subregions in the coronal plane (Fig. 2E–G), and post-PLI Nissl stains were used to further identify the detailed lamination of the ERC from human brain #1 (Fig. 3B).

### Segmentation of Medial Temporal Subregions

In keeping with other anatomic descriptions of the MTL (Witter and Amaral 1991), proximal/distal refers to nearer/further from the dentate gyrus (e.g., CA2 is proximal to CA1, and CA1 is distal to CA2), and superficial/deep refers to nearer/further from the hippocampal sulcus (e.g., the molecular subiculum is superficial to the subicular pyramidal layer in Fig. 3A on the far right). Radial/tangential means perpendicular/parallel to the adjacent cortical surface or hippocampal sulcus (e.g., the yellow arrow in Fig. 3B represents radial orientation whereas the superficial red arrows in Fig. 3A denote a tangential orientation), and transverse/longitudinal means within-plane/through-plane on a coronal section (e.g., the superficial red arrows in Fig. 3A represent a transverse orientation, whereas the red cross hair in the presubiculum in Fig. 3A corresponding to the red arrows in Fig. 3C represents a longitudinal orientation).

To facilitate visual analysis of pathways, we segmented the medial temporal subregions on transmittance images from the coronally sectioned temporal lobes (Figs 2E–G, 3B, and 7). Myelin generally appears dark on transmittance images, and regions with less densely packed myelin, such as the CA field pyramidal cell layers, are overall hypointense. Cell bodies also appear dark, but they are not as dark as myelin on transmittance images, and only large cells are visible, limiting the ability to use conventional cell morphology-based delineations of the boundaries between CA fields and hippocampal layers. Instead, we used a rule-based system applied to the transmittance images as described below. The uncus and most anterior portions of the hippocampal head are extremely complicated (Ding and Van Hoesen 2015) and were not comprehensively investigated as part of this study. In general, when boundaries were unclear on a given section, adjacent sections were used to aid in the interpretation. We approximated all borders between subregions as orthogonal to the cortical and hippocampal sulcal surface. Segmentation was not performed on the sagittal images; instead, the reformatted coronal blockface image was used to judge the subregion by analogy with the left-sided direct coronal sections when needed.

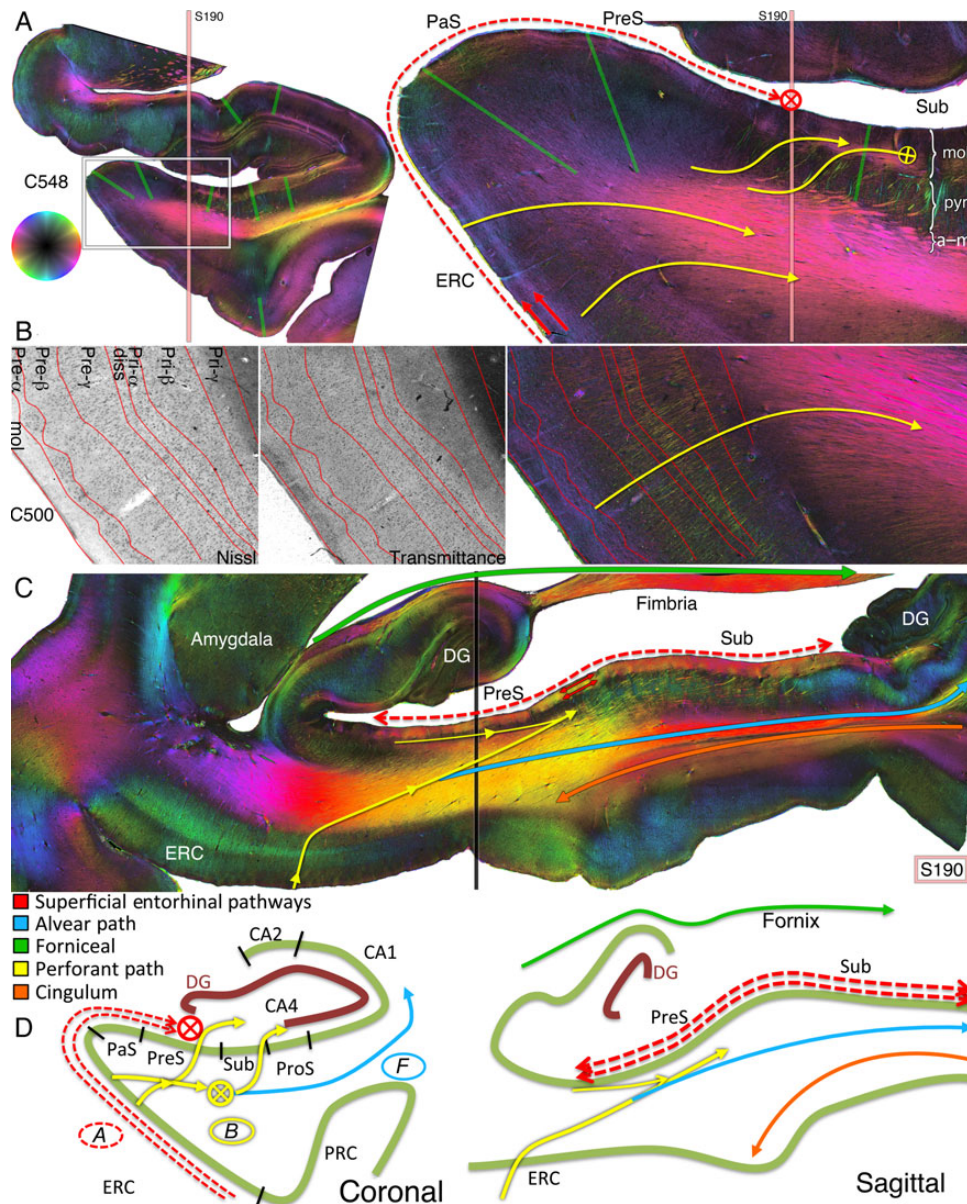


**Figure 3.** Entorhinal pathways and the angular bundle. (A) Coronal PLI at the level of the posterior hippocampal head of the left hemisphere of brain #1. The approximate localization of sagittal section S190 (shown in C) is indicated by peach vertical line. The green boundaries correspond to the subregion demarcations on the transmittance images from Figure 2E. The hue on the color wheel indicates the direction of the in-plane fiber orientation (see Supplementary Fig. 1), and the brightness/darkness of the color (e.g., more peripheral/central in the color wheel) indicates a primarily in-plane/through-plane orientation. Arrows with cross hairs denote a through-plane orientation. Best seen on the zoomed in coronal section from the box on the left are dual superficial entorhinal pathways (red arrows) running tangentially throughout the ERC to the parasubiculum and presubiculum. Both project longitudinally in the molecular layer of the presubiculum (red cross hair), confirmed on sagittal plane S190 of the right hemisphere in (C). In yellow are medial entorhinal projections to the angular bundle (lower 2 curvilinear yellow arrows) and from the angular bundle through the presubiculum into the molecular subiculum (top yellow sigmoidal arrows). Subicular lamination on the far right is indicated as mol, molecular; pyr, pyramidal; a-m, alvear/multiforme. (B) A slightly more anterior section (C500) with Nissl staining performed after PLI for visualization of cell bodies. Lamination of the ERC derived from the Nissl stain is superimposed on the transmittance and fiber orientation maps. Perforant pathway fibers originate in approximately layer Pre- $\alpha$  of the ERC and radially project to the angular bundle (yellow curved arrow). (C) Sagittal PLI slice S190 from the right hemisphere of brain #1 at the approximate location indicated by the vertical peach line in A. The approximate localization of the coronal section from the left hemisphere in A is indicated by the vertical black line on this right sagittal section. Red arrows highlight the presubicular longitudinal components of the superficial entorhinal pathways from A. The lower yellow arrow signifies perforant path projections from the medial ERC, through the angular bundle, and toward the presubiculum and subiculum. More superiorly is a longitudinal entorhinal pathway (thin yellow arrow) running in the pyramidal layer of the presubiculum, depicted as the yellow ellipses in Figure 4. The green arrow depicts fibers projecting to the fimbria; in blue is the alvear bundle to the posterior hippocampus; and in orange is the cingulum bundle within the parahippocampal gyrus (see Supplementary Fig. 3). (D) Diagrammatic representation of entorhinal pathways in the coronal and sagittal planes.

We segmented subregions according to the following guidelines primarily on the coronal transmittance images (Figs 2E-G, 3B, and 7):

1. Dentate gyrus
  - (a) The granular cell layer was a thin dark intensity stripe on transmittance images.

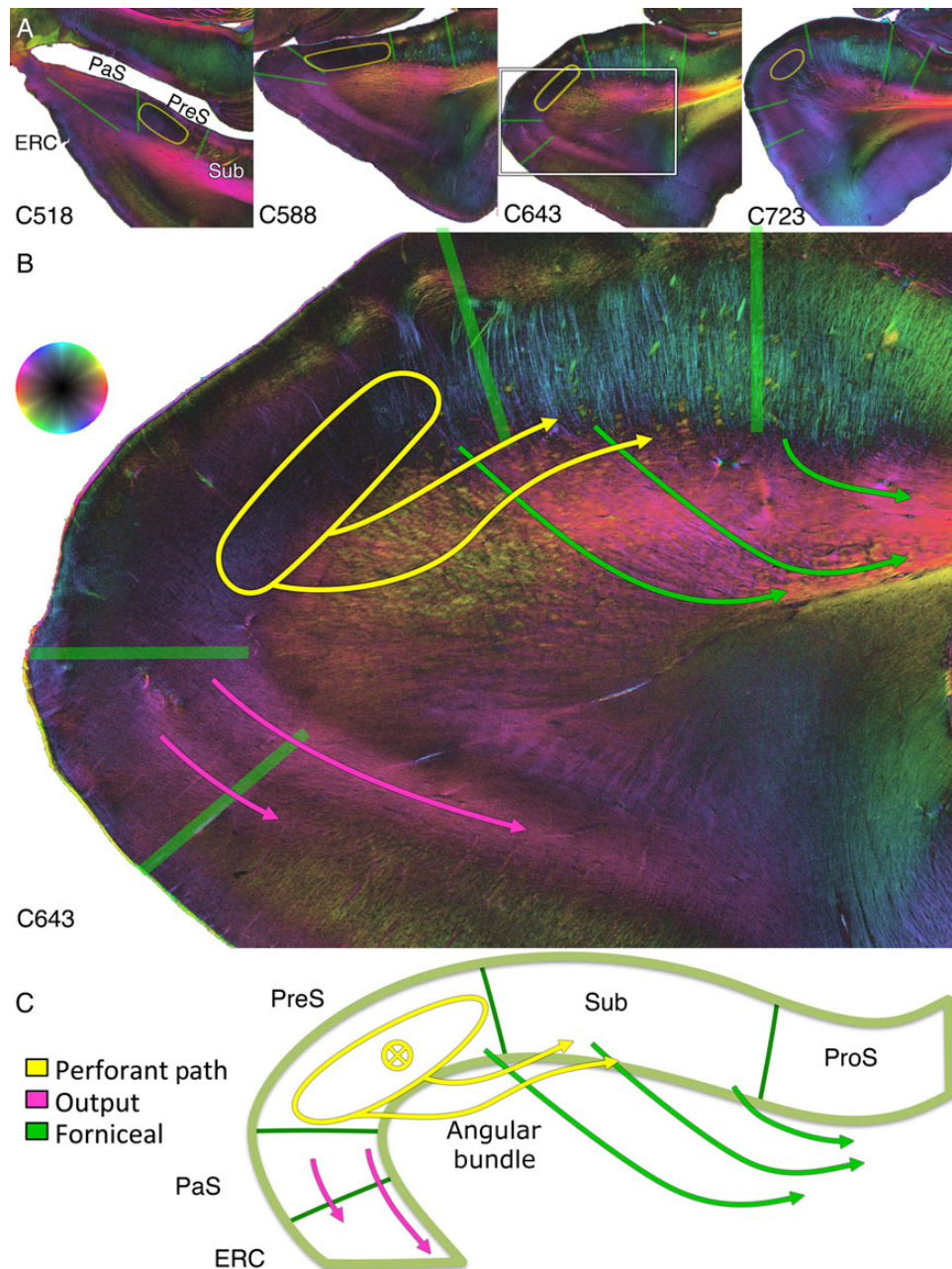


**Figure 4.** Resolving crossing fibers in the parahippocampal gyrus. (A) Coronal sections anteriorly (C518) to posteriorly (C723). (B) Zoom in on the white box on C643. (C) Schematic of crossing fiber bundles. Yellow ellipse: the ERC most anteriorly (C518) projects to a longitudinal bundle that extends through the entire presubiculum within the pyramidal cell layer, deep to the molecular layer (see also Fig. 7 for the dark signal underneath the presubicular label). From and deep to this, obliquely oriented thick perforant pathway bundles can be seen extending to the subiculum proper (yellow arrows). Green arrows: a crossing curvilinear pathway projects from the subiculum to the parahippocampal gyrus and then turns to enter the alveus, representing subicular fibers projecting to the fornix (see also Fig. 8B). Thus, PLI can discern that the subicular output (dark purple fibers in C643) and perforant input fibers (yellow-green fibers in C643) cross one another subjacent to the subiculum, confirmed on the spotlight images of [Supplementary Figure 4](#). Pink arrows: distally in the parasubiculum are CA1 and subiculum output fibers extending to the entorhinal region.

- (b) The relatively less intense molecular layer extended from the granular cell layer to the hippocampal sulcus. Lamination of the outer, middle, and inner thirds of the dentate molecular layer was evident on the color fiber orientation maps (Figs 6B and 8C).
  - (c) The relatively less intense polymorphic layer was identified as the thin cell-sparse layer subjacent to the granular cell layer.
2. CA4
    - (a) Large cell bodies populated this otherwise hypointense region filling the hilus.
    - (b) The distal border was defined as a gentle U-shaped curve stretching from the medial to lateral blade of the dentate gyrus.
  3. CA3
    - (a) Large dense pyramidal cell bodies occupied the central hypointense portion of this layer. At the CA3/CA2 boundary, the pyramidal cell layer became more dense, compact, and narrower.
    - (b) Lamination was well seen on the color fiber orientation maps (Fig. 6A).
  4. CA2

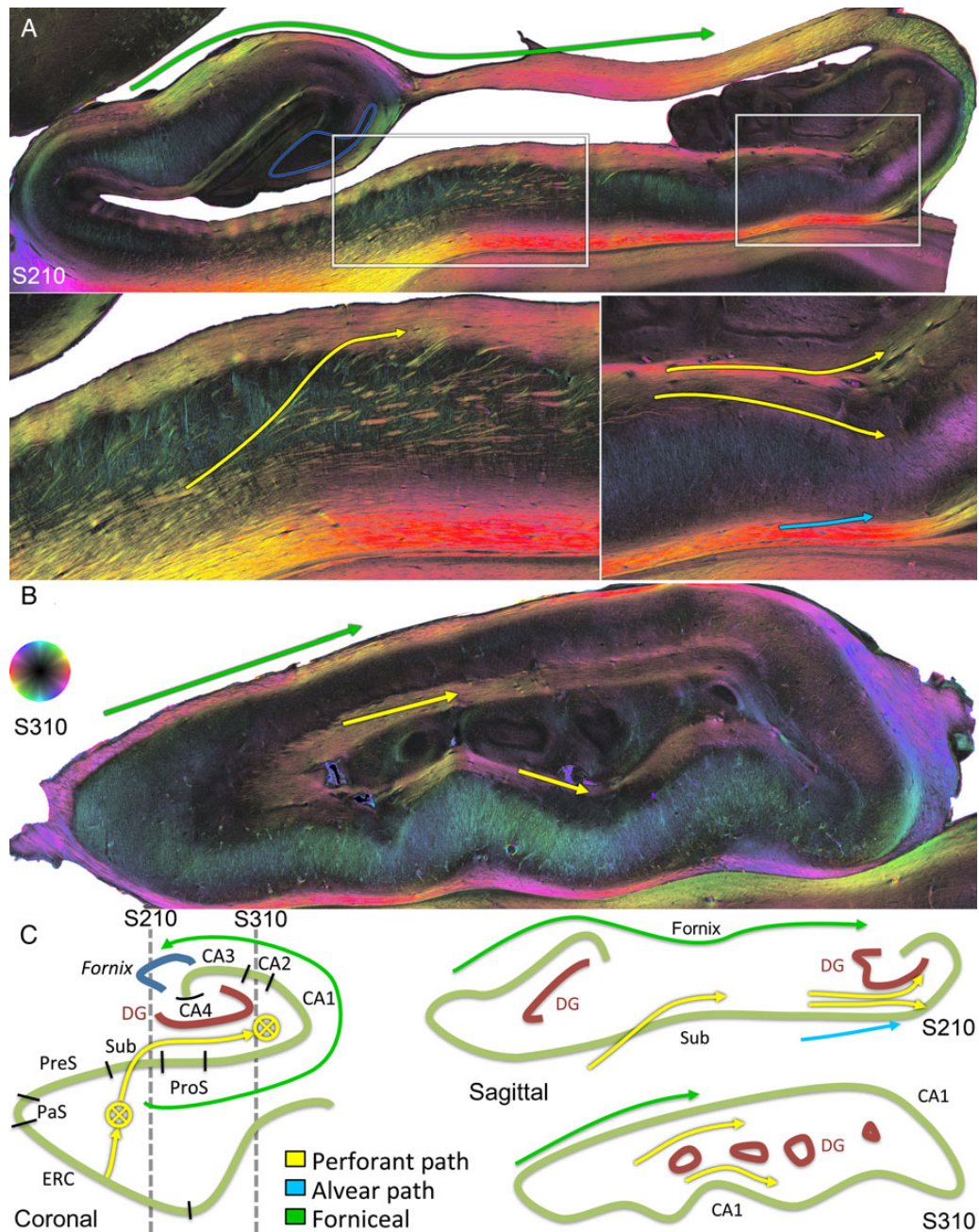


**Figure 5.** Perforant path system longitudinally. (A) Medial sagittal section through the subiculum indicated by the medial gray dotted line in C (S210). The bottom left inset shows thick steeply longitudinal bundles of perforant fibers ascending through the subiculum (yellow arrow). The bottom right inset shows perforant path fibers going posteriorly to the hippocampal tail, targeting the outer one-third of the dentate superiorly and CA1 inferiorly (yellow arrows). Alvear fibers can be seen coursing into CA1 (light blue arrow). Superiorly, the alveus and fimbria contain extensive longitudinal fibers heading to the fornix (green arrow). (B) Lateral sagittal section indicated by the more lateral gray dotted line in C (S310). Extensive longitudinal fibers occupy CA1 lacunosum-moleculare (corresponding to the relatively dark portions on the coronal images from Fig. 8B,C, and yellow encircled regions in Supplementary Fig. 5). The alveus also contains extensive longitudinal fibers (green arrow). (C) Medial (S210) and lateral (S310) sagittal schematics on the right, with the corresponding coronal schematic cross-referenced by the gray dotted lines on the left.

- (a) The boundary to CA1 was defined by the expansion of the central hypointense layer, representing the wider pyramidal cell layer of CA1.
5. CA1
    - (a) The border to the prosubiculum is described below.
    - (b) Lamination also best defined on the color fiber orientation maps (Figs 6A, 7, and 8B,C). Progressing from deep to superficial:
      - (i) the alveus, which contains mostly longitudinal fibers proximally,
      - (ii) stratum oriens, which contains tangential fibers (Fig. 6A),
      - (iii) the pyramidal cell layer, which demonstrates extensive radial fibers (Fig. 8B,C),
      - (iv) stratum radiatum, which proximally contains Schaffer collaterals (Fig. 6A) and distally contains tangential perforant fibers that arc deep into the pyramidal layer (Fig. 8C), and

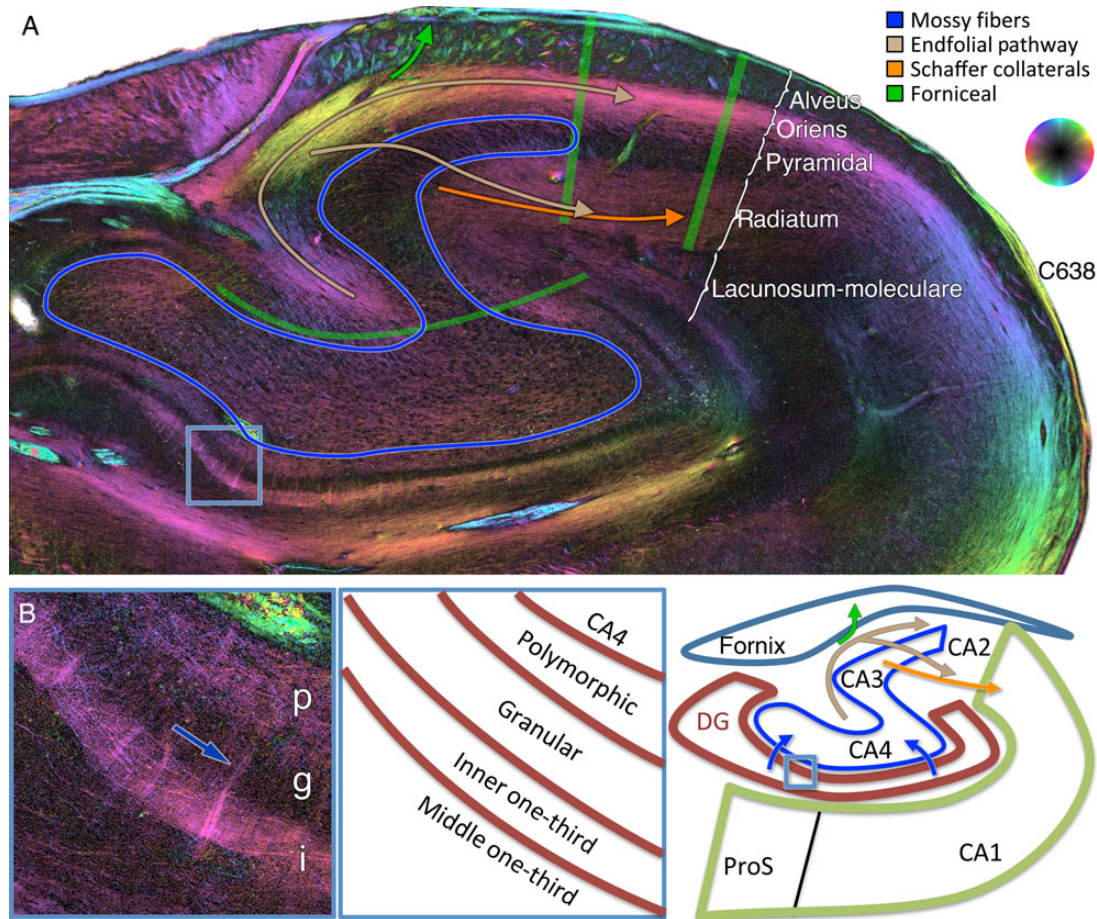


**Figure 6.** Dentate fibers, mossy fibers, endfolial pathway, and Schaffer collaterals. (A) Coronal PLI at the level of the hippocampal body showing a relatively diminished color orientation in fields CA4 and CA3 pyramidal cell layers, circumscribed in blue, representing the unmyelinated target of the mossy fibers. Endfolial fibers originate in CA4 (upper light brown curvilinear arrow) and project to stratum oriens. The Schaffer collaterals originate in CA3 (orange arrow) and project to the stratum radiatum. Fibers project from the endfolial pathway to the Schaffer collaterals (lower light brown sigmoidal arrow). The overlying alveus contains largely longitudinal fornical fibers (see Figs 3C and 5A,B). (B) Zoomed in section on the medial and inferior dentate gyrus indicated by the blue box in A at the bottom left. p, polymorphic layer, g, granular cell layer, and i, inner one-third of the dentate gyrus. This demonstrates tangential fibers in the polymorphic layer and inner one-third of the dentate gyrus, likely representing mossy cell associational fibers. Some subtle fibers can be seen traversing the granular layer to bridge these 2 layers (dark blue arrow).

- (v) stratum lacunosum-moleculare, which contains tangential and longitudinal perforant fibers that cross the hippocampal fissure en route to the dentate molecular layer.
6. Subicular complex [each component contains a molecular layer superficially, a pyramidal cell layer centrally, and an alvear/multiform layer in the deepest portion, seen in Fig. 3A at the far right and Fig. 8B at the far left; (Stephan 1975; Ding 2013)].
- Prosubiculum—An oblique wedge of dark intensity on transmittance images defined the entire prosubiculum (Fig. 2E–G).
  - Subiculum proper—The proximal/distal borders were clearly defined by the conspicuous prosubiculum/presubiculum boundary described above/below. A few superficial hypointense cell islands were present in anterior slices (Fig. 2E).
  - Presubiculum—The deeper pyramidal layer contained dark intensity indicative of myelin on all coronal sections (green asterisks in Fig. 2E–G), fully defining the presubiculum.
  - Parasubiculum—Less intense darkening in the deeper pyramidal layer defined the extent of the parasubiculum.
7. ERC
- To determine entorhinal lamination, cresyl violet Nissl staining was performed on coronal section 500 from human brain #1 after PLI measurement (Fig. 3B). The Nissl stain was inspected under a camera lucida microscope and the borders between the cellular layers demarcated according to the convention of Braak (1980). The equivalent Insausti terminology would be as follows: I = mol(ecular) layer, II = Pre- $\alpha$ , III = Pre- $\beta$  and Pre- $\gamma$ , IV = diss(ecans), V = Pri- $\alpha$ , VI = Pri- $\beta$ , and Pri- $\gamma$  (Insausti et al. 1995).
  - Throughout the slices containing the hippocampal head, a very thin stripe of hypointensity at layer V/Pri- $\gamma$  [Figs 2E, F and 3B, one layer deep to the lamina dissecans (Braak 1980; Insausti et al. 1995; Heinsen et al. 1996)] formed the distal border. The collateral sulcus was deep on coronal sections from all human specimens, so the border along the collateral sulcus was not shifted (Insausti et al. 1998). Anteriorly, where the hippocampal sulcus was fused, we segmented the ERC extending superiorly up to the semiannular sulcus. Posteriorly, the boundary separating the entorhinal, perirhinal, and parahippocampal

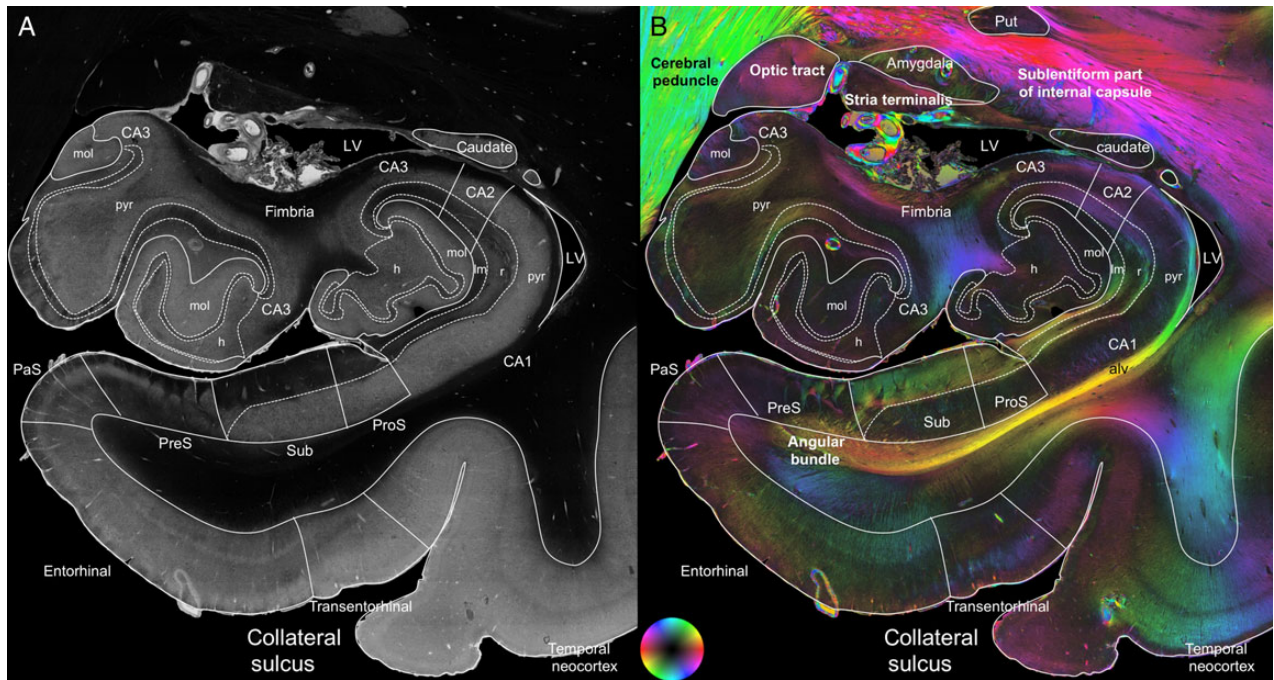


**Figure 7.** Coronal PLI of hemisphere #3. (A) Transmittance image of an anterior left coronal section from brain #2. (B) Corresponding color orientation map of section shown in A. alv, Alveus; CA, cornu ammonis; h, hilus; mol, molecular layer; lm, stratum lacunosum-moleculare; LV, temporal horn of lateral ventricle; PaS, parasubiculum; PreS, presubiculum; ProS, prosubiculum; Put, putamen; pyr, pyramidal layer; r, stratum radiatum.

cortices was difficult to identify, and the posterior entorhinal border was approximated as 16 sections (~1.1 mm) posterior to the posterior most uncus.

### Analysis of Fibers

Combining visual analyses of coronal and sagittal sections enabled us to take advantage of the extremely high in-plane resolution of PLI to optimally detect the superior–inferior and right–left trajectories in the coronal images, and superior–inferior and anterior–posterior trajectories in the sagittal images. Our primary interpretation was based on the coronal images, in which we identified the orientation of myelinated fibers by examining the color-coded fiber orientation maps (the explanation of color orientation is provided in [Supplementary Fig. 1](#)), examining the color as well as the image texture (e.g., numerous lines pointing in one direction). Dark regions on transmittance images that were not cell bodies were generally considered to represent myelin. PLI is maximally sensitive for fibers oriented in-plane; on coronal images, fibers oriented through-plane (i.e., along the anterior–posterior axis of the hippocampus) would appear dark on the transmittance images, but show reduced or no color orientation. The sagittal images were used in this case to confirm through-plane orientation of any pathway, and the appropriate sagittal section was identified by visually comparing the block-face volumes from the coronally and sagittally sectioned hemispheres. Combining all of this knowledge of PLI with our subregion segmentation, we visually identified the major pathways that reflect known connectivity in animal studies. A pathway is described when 3 experienced neuroanatomists (M.M.Z., N.P.-G., and K.Z.) agreed on the interpretation of a fiber bundle. A known limitation of PLI and MRI-based fiber tracking is that we cannot determine, based solely on the image, whether a fiber, or a fiber bundle, is entering or leaving the hippocampus

(i.e., which way is anterograde/retrograde), so we used animal studies to guide the interpretation.

We describe fiber bundles associated with following different pathways (Fig. 1):

1. Perforant path system.
2. Pathways in and from the fascia dentata.
3. Endfolial path and Schaffer Collaterals.
4. CA1/subiculum to ERC.

### In Vitro Receptor Autoradiography

To confirm the location of mossy fibers, we performed receptor autoradiography of kainate receptor-binding sites in the human hippocampus since it has been demonstrated that kainate receptors are found at very high density in the mossy fiber termination fields (Zilles et al. 2002). Thus, kainate receptor distribution can be used to corroborate the identification of the mossy fiber termination as visualized by PLI. Unfixed deep frozen human brains were sectioned in the coronal plane with a section thickness of 20  $\mu\text{m}$ . Sections were mounted on glass slides and incubated in a 50-mM Tris-citrate buffer (pH 7.1) containing 10 mM calcium acetate and 8 nM [ $^3\text{H}$ ]kainate in the presence of (as a displacer for the determination of non-specific binding), or without, 100  $\mu\text{M}$  kainate. Radiolabeled sections were exposed against tritium-sensitive films and processed densitometrically. The binding site densities were calculated in fmol/mg protein and color-coded. For details of the autoradiographic procedure, see Zilles et al. (2002).

### Magnetic Resonance Imaging

A single male 26-year-old right-handed subject was consented in accordance with the Stanford Institutional Review Board and imaged on a GE 750 HDx 3.0 T 60 cm bore magnet with 60 min of

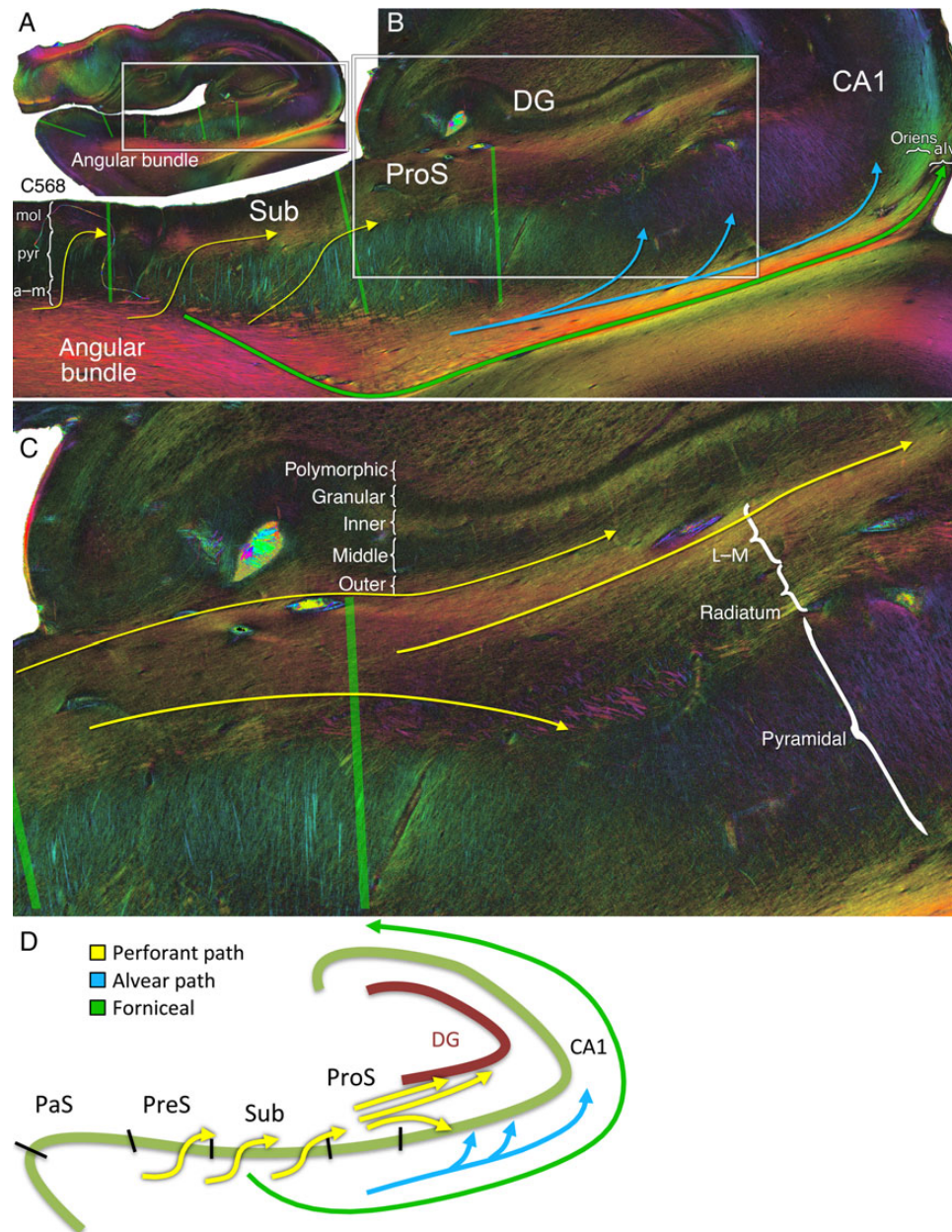


**Figure 8.** Perforant path system in-plane. (A) Angular bundle fibers projecting to the more posterior portion of the hippocampal head. (B) Perforant (yellow), alvear (light blue), and forniceal (green) pathways, shown at a higher magnification (see box in A). Yellow arrows: Sigmoidal perforant pathway fibers of varying obliquities can be seen extending from the angular bundle, through the subiculum, and into the deeper part of the molecular layer of the subiculum. Light blue arrows: Deeper angular bundle alvear pathway fibers extend subjacent to the prosubiculum and into the stratum oriens where they penetrate the pyramidal layer of CA1. Green arrows: output fibers emanating from the subiculum obliquely cross the fibers of the angular bundle en route to the parahippocampal gyrus and then alveus, ultimately to reach the fornix. Subicular lamination is indicated as mol, molecular; pyr, pyramidal; a-m, alvear/multiforme. CA1 lamination is indicated as oriens, stratum oriens; alv, alveus. (C) Higher magnification of the box shown in B depicting the dentate layers (polymorphic, granular, and inner/middle/outer thirds of the molecular layer) and CA1 lacunosum-moleculare (L-M), radiatum, and pyramidal layers. Perforant pathway bifurcation: Tangential perforant pathway fibers in the superficial molecular layer of the subiculum extend into the superficial L-M and project to the outer one-third and to a lesser degree to the middle one-third of the dentate molecular layer (yellow arrows, top). Fibers in the deeper molecular layer of the subiculum continue in a tangential manner in the radiatum and then turn inferiorly to penetrate deeper into the CA1 pyramidal cell layer (yellow curved arrow, bottom). (D) Graphical depiction of the perforant, alvear, and forniceal pathways.

diffusion tensor imaging (DTI) as part of our prior work, processed in an identical manner as previously described (Zeineh et al. 2012). Briefly, an axial diffusion-weighted sequence of 70 directions at  $b = 1500 \text{ mm}^2/\text{s}^2$  and 10  $b = 0 \text{ mm}^2/\text{s}^2$  images at an isotropic resolution of 1.4 mm covering the entire temporal lobe was acquired 7 times. Images were eddy-current, distortion, and motion coregistered using the FMRIB Software Library (FSL)

5.0 (Jenkinson et al. 2012). We generated tractography using “MRtrix3” (J-D Tournier, Brain Research Institute, Melbourne, Australia, <https://github.com/MRtrix3/mrtrix3>), which utilizes a response function generated from the diffusion-weighted images to perform constrained spherical deconvolution, resulting in a fiber orientation distribution (Tournier et al. 2008). Bidirectional probabilistic streamline tractography was subsequently

performed between the ERC and CA1–3 using the following parameters: maximum number of tracks = 2000, step size = 0.07, cut-off value = 0.2, initiating cutoff = 0.2, and minimum track length = 3.5 mm. The resulting tracts were filtered further by excluding those that pass through the surrounding cerebrospinal fluid and truncating those that exceed a whole hippocampus mask. This same subject underwent consent and structural imaging as part of another study at 7 T on a GE 950 HDx magnet (Zeineh et al. 2014), and the 3D  $T_2$ -weighted fast spin-echo ( $0.7 \times 0.7 \times 0.7$  mm) from this study was used as a backdrop for displaying tracks, manually aligning both with 3D Slicer ([www.slicer.org](http://www.slicer.org)). These data were used for [Supplementary Figure 7](#).

## Results

### Vervet Monkey Validation

Polarized light microscopy demonstrates all of the perforant pathway elements established in the monkey literature (Fig. 1, bottom left and [Supplementary Fig. 2](#)): The superficial entorhinal projection to the parasubiculum and presubiculum (A); perforant path system originating in the ERC (B), penetrating the subiculum (C), and projecting to the dentate gyrus (D), and CA fields (E); as well as the alvear component (F). Other pathways directly evident include Schaffer collaterals extending from CA3 to CA1 as well as hilar and subicular projections to the fornix (Fig. 1, bottom right). The endfolial pathway can be visualized (Fig. 1, bottom right, light brown arrow; [Supplementary Fig. 2](#), coronal slices C582 and C675, light brown arrows).

### Perforant Pathway

The present observations demonstrate the following components of the perforant path system in the human brain.

#### A. Superficial Entorhinal Projection

The “sublamina supratentorialis” was identified as a tangential bundle throughout the superficial molecular layer (layer I) of the ERC (Fig. 3A, right panel, red arrows). From there, a thick longitudinal projection is clearly visible on the sagittal images in the superficial and proximal presubiculum (Fig. 3C, red arrows). Just deep to this superficial projection was a second tangential projection with even greater thickness in the coronal plane, demonstrating a parallel trajectory to the parasubiculum (Fig. 3A, deeper red arrow). This slightly deeper pathway projected to a longitudinal component throughout the entire parasubiculum and presubiculum (Fig. 3C, deeper red arrow).

#### B. ERC to Angular Bundle

Radial fibers emanated from all entorhinal layers, with the exception of the molecular layer, and are found in the angular bundle located in the white matter of the medial parahippocampal gyrus (Figs 3A,B, 4, 7, and 8). Dense longitudinal fibers were clearly evident throughout the bulk of the anterior parahippocampal gyrus and superior portion of the posterior parahippocampal gyrus on the sagittal sections, extending toward the subicular complex (Fig. 3C, lower yellow arrow). These fibers were separable from the cingulum bundle more inferiorly in the parahippocampal gyrus (see [Supplementary Fig. 3](#)). Additionally, the anterior and proximal ERC sent a longitudinal pathway to the presubicular pyramidal layer (Fig. 4, yellow oval; Fig. 3C, upper thin yellow arrow; Fig. 7B, directly under the presubiculum label), deeper than both longitudinal projections of pathway A as described above. This deeper longitudinal pathway extended along the

presubiculum, and fibers from it enter the parahippocampal gyrus as seen in the coronal plane (Fig. 4, C643). From there, thick clumps of fibers can be seen heading toward and into the subiculum (Fig. 4, C643, yellow arrows). These fibers exhibit decreased conspicuity laterally in the posterior parahippocampal gyrus because of crossing of curvilinear subicular fibers projecting to the alveus and fornix (Fig. 4, C643, green arrows). At the crossing point in the mid-parahippocampal gyrus, the yellow-green perforant fibers intersected dark purple subicular fibers heading to the alveus, producing an intermediate red coloration by superimposition of fibers in the 70- $\mu$ m thick sections, but perforant and subicular fibers can still be differentiated. This separation is confirmed on spotlight images that highlight the perforant separate from the subicular fibers (see [Supplementary Fig. 4](#)).

#### C. Angular Bundle Perforation Through the Subiculum

Sigmoidal fibers perforated the presubiculum, extending from the angular bundle medially to the molecular layer of the presubiculum, and projected toward molecular layer of the subiculum laterally (Fig. 3A, upper yellow sigmoidal arrow; Figs 7 and 8B).

Angular bundle fibers also demonstrated an extensive projection through the subiculum proper and prosubiculum (Figs 7, 8, and [Supplementary Fig. 5](#)). The course of this portion of the pathway was largely sigmoidal, and a great number of individual fibers were entirely in-plane in the coronal sections (Fig. 8B, yellow sigmoidal arrows; [Supplementary Fig. 5](#)). The sigmoidal bundles were dense in particular throughout the middle-to-posterior hippocampal formation (see [Supplementary Fig. 5](#)). In addition, separate groups of obliquely sectioned longitudinal fibers from the parahippocampal gyrus (Fig. 4, yellow arrows, fibers projecting through the deep subiculum, also in Fig. 7) continue as thick steeply longitudinal bundles clearly visible in sagittal sections (Fig. 5A, bottom left, yellow arrow). All of these perforant fibers extended to the molecular layer of the subiculum and prosubiculum (Fig. 8B and [Supplementary Fig. 5](#)). From there, a large bundle of myelinated fibers continued longitudinally throughout the stratum lacunosum-moleculare along the long axis of the hippocampus (see [Supplementary Fig. 5](#), encircled yellow region C600, C663, and C750; Fig. 5B, yellow arrows).

#### D. Perforant Path to Dentate Gyrus

In the stratum lacunosum-moleculare, fibers crossed the hippocampal fissure to project to the outer and middle thirds of the dentate molecular layer in the coronal and sagittal planes (Fig. 5A, bottom right panel, upper yellow arrow; Fig. 8C, upper yellow arrows). The superficial fibers were dense, whereas slightly deeper dentate fibers appeared less dense in both section directions.

#### E. Perforant Path to CA Fields

In the stratum radiatum, curvilinear thick fibers arced distally (inferiorly) toward the CA pyramidal cell layer in both the coronal (Fig. 8C, lower yellow arrow) and sagittal planes (Fig. 5A, bottom right, lower yellow arrow).

#### F. Alvear Path

In the coronal plane, fibers from the deep angular bundle can be seen arcing in a curvilinear fashion deep to the subiculum, and then toward the pyramidal layer of CA1; these alvear fibers exhibit a greater density than those in the vervet monkey (Figs 3A,D and 8B, light blue arrows, compare with [Supplementary Fig. 2](#)). In the sagittal plane, similar fibers can be seen projecting to CA1 of the hippocampal tail (Fig. 5A, bottom right,

light blue arrow). In the very anterior hippocampus, anteromedial entorhinal fibers project directly to CA1 via a similar approach both superiorly and inferiorly (see [Supplementary Fig. 6](#), light blue arrows). At this anterior level, where the hippocampal sulcus is fused medially and the ERC is in close proximity to the hippocampus, the perforant and alvear pathways can be seen in completion on one coronal PLI section, all the way from the ERC to the dentate molecular layer and stratum lacunosum-moleculare (see [Supplementary Fig. 6](#)).

#### Comparison with DTI

In vivo diffusion tensor probabilistic tractography on a different subject utilizing constrained spherical deconvolution can visualize longitudinal projections of the angular bundle best seen on the sagittal plane (see [Supplementary Fig. 7](#), left) as well as perforant, alvear, and fornical components in the coronal plane (see [Supplementary Fig. 7](#), right).

#### Pathways in and from the Fascia Dentata

Two pathways could be determined:

1. Two thin stripes of myelinated fibers were seen at either side of the granule cell layers, one lining the polymorphic layer and the other the inner one-third of the molecular layer (Figs 6B and 8C, and [Supplementary Fig. 8](#)). These fibers, which may represent mossy cell axons ([Amaral et al. 2007](#)), run tangentially to the dentate granule cell layer in both the

coronal and sagittal planes (Fig. 6B and [Supplementary Fig. 8](#)), indicating a nonpreferential spatial course. Additionally, radial components are visible and bridge the granular cell layer (Fig. 6B and [Supplementary Fig. 8](#), dark blue arrows).

2. A region characterized by a relative absence of signal in PLI indicating a low or lack of myelin content was found in the hilus, and this extended distally lateral to the endfolial pathway up to the CA3/CA2 margin (Figs 5A and 6A, dark blue outlines in the hilus). This location correlates with a site of selectively high kainate receptor density specific for mossy fiber termination sites (Fig. 9). Therefore, we inferred this relative absence of PLI signal together with high kainate receptor density as representing the course and termination field of mossy fibers, an unmyelinated pathway projecting from the dentate granular layer to the hilus and CA3 ([Hamlyn 1962](#); [Lim, Blume, et al. 1997](#); [Kress et al. 2008](#)).

#### Endfolial Path and Schaffer Collaterals

A meshwork of fibers was seen to originate in CA4, converge in the upper hilus, and extend into the stratum oriens of CA3 (Fig. 6A, upper light brown curvilinear arrow); this is probably the correlate of the endfolial pathway ([Lim, Mufson, et al. 1997](#); [Parekh et al. 2015](#)). A thick band of fibers originates in CA3 and extends distally in the stratum radiatum to CA1 (Fig. 6A, orange arrow); this is likely the correlate of the Schaffer collaterals ([Kondo et al. 2009](#)). Many of the distal endfolial fibers crossed

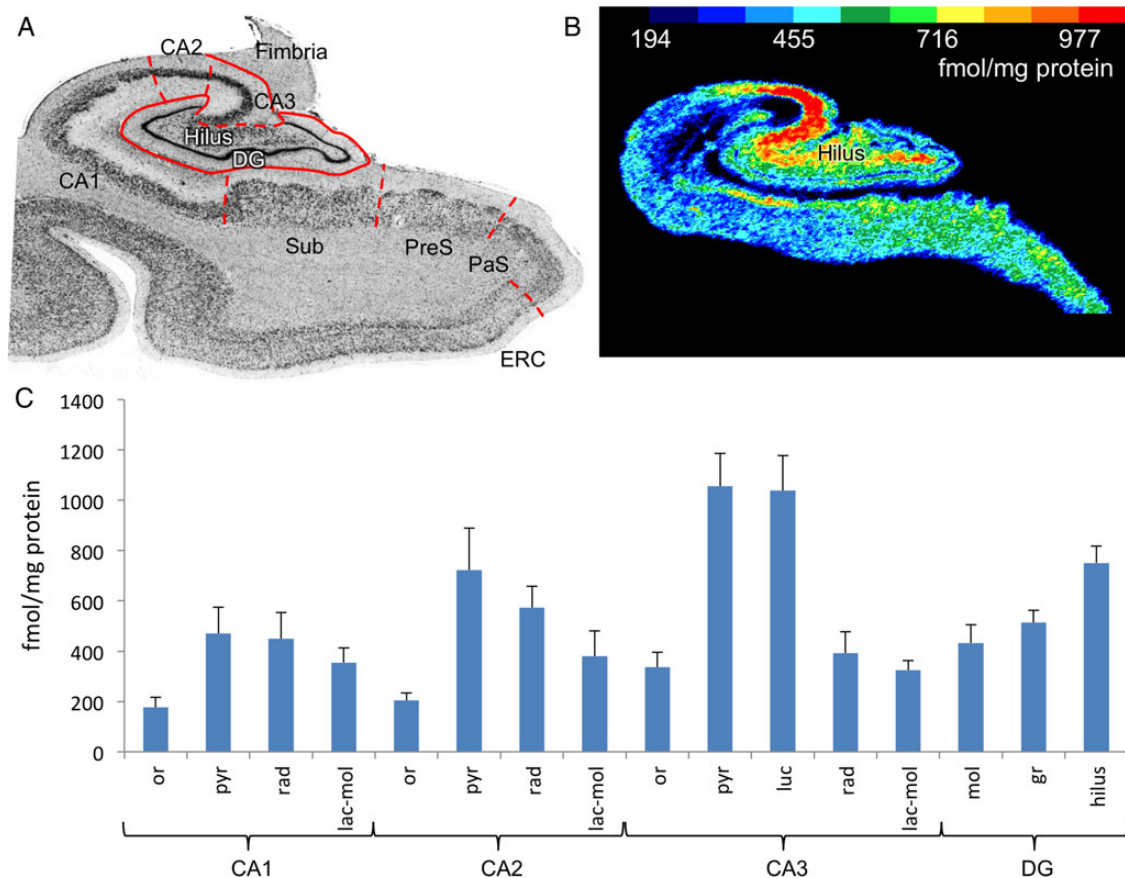


**Figure 9.** Kainate receptor autoradiography. (A) Nissl stain of one representative medial temporal section. (B) Kainate autoradiography. (C) Mean concentration of kainate receptors across hippocampal subfields and layers ( $n = 5$ ). The highest concentration is in the pyramidal and lucidum layers of CA3 followed by the hilus. or, oriens; pyr, pyramidal; rad, radiatum; lac-mol, lacunosum-moleculare; luc, lucidum; mol, molecular; gr, granular; hilus, both the polymorphic layer of dentate gyrus and CA4.

the pyramidal layer of CA3 and appeared to run together with the Schaffer pathway (Fig. 6A, lower light brown sigmoidal arrow). Fibers visualized heading toward the alveus and fornix emanate from the stratum oriens (Fig. 6A, green arrow) and extend longitudinally (Figs 3C top and 5A,B top, green arrows). The color orientation maps clearly delineate the distinction proximally between the longitudinally oriented alveus projecting to the fornix and the tangentially oriented stratum oriens containing the endfolial path (Fig. 6A).

### CA1/Subiculum to ERC

The projection from the subicular complex and CA1 back to the ERC forms a curvilinear pathway extending through the parasubiculum into the ERC, with both a deep and more superficial component (Fig. 4, C643, pink arrows), similar to that seen in monkey tracer studies (Saunders and Rosene 1988).

## Discussion

In this study, we have used high-resolution polarized light microscopy to define the course and architecture of the perforant path system as well as of all other key pathways in the MTL. After validating our technique by examining the known anatomy of the perforant path system in the monkey, we established the normative anatomy in humans. This should provide an anatomic “ground truth” for methods, such as DTI-based tractography, and a reference for studies of the perforant path system in Alzheimer’s disease and of hippocampal circuitry in modeling of mnemonic function and impairment.

The human perforant path system has been previously studied with high-resolution *ex vivo* DTI as well as with a combination of structural MRI and myelin-stained histological sections (Augustinack et al. 2010). Portions of the perforant path system were shown that are similar to our findings: Projections from the ERC to the angular bundle and subiculum, and projections from the subiculum to the dentate gyrus and CA fields. However, these efforts had difficulty capturing the continuity from the ERC to the dentate gyrus and the CA region because of crossing fibers in the presubicular and subicular regions and an inability to detect crossing through the hippocampal fissure. These difficulties were avoided in the present study by ultra-high-resolution PLI, which allows the direct visualization of myelinated fibers and the tracking of crossing fibers through the angular bundle and the presubicular and subicular region. Similarly, we capture the central portion of the perforant path system as has been done with *in vivo* studies (Yassa et al. 2010), without the requirement of any modeling or prior knowledge of fiber directions. Finally, in comparison with all of this prior work, we show many more components of the perforant path system by directly illustrating the 3D orientation of the anatomic fibers and fiber bundles.

In addition to confirming the key connections expected from animal data, new insights are provided by this examination of vervet monkey and human tissue. The superficial entorhinal pathway is more extensive in humans than expected according to the monkey data (Witter and Amaral 1991) and limited human data (Braak 1980): 2 tangential layers run along the entorhinal surface, the deeper of which has an extensive longitudinal pathway through the parasubiculum and presubiculum. The alvear pathway is also unexpectedly prominent and significantly larger in the human in comparison with the monkey, having a great number of fibers projecting to CA1, confirming the limited evidence from other *ex vivo* examinations of human tissue (Hevner and Kinney 1996). The other elements of the

perforant path system demonstrate multiple trajectories of interwoven axonal bundles. The angular bundle was identified to have the expected transverse curvilinear projection to the subiculum, but there was an additional set of thick bundles running steeply longitudinally in the parahippocampal gyrus, as well as a dense band of longitudinal fibers in the deep presubicular pyramidal layer. More laterally in the parahippocampal gyrus, the fibers of the angular bundle intersected curvilinear subicular fibers projecting to the alveus and fornix. In spite of the extremely high in-plane resolution of 1.3  $\mu\text{m}$ , each pixel can contain crossing of fibers because of the 70- $\mu\text{m}$  thickness of the section that is captured by the optical depth of the microscope. While crossing fiber effects can occur within a pixel, they are much less frequent than in the much larger pixels of DTI. Therefore, fewer pixels contain multiple fiber bundles at this high resolution, enabling us to tease apart these crossing pathways and decipher the complexity of the parahippocampal gyrus. The pattern of multiple perforant pathway elements continued into the subiculum proper: While a great number of fibers showed a transverse sigmoidal penetration through the pyramidal cell layer, numerous thick bundles continued longitudinally from the parahippocampal gyrus through the subicular pyramidal layer. The perforant pathway then took the expected trajectory in the stratum lacunosum-moleculare: Either continuing to terminate in the dentate gyrus or arcing downward in the stratum radiatum toward the CA fields (Witter and Amaral 1991). The extensive longitudinal projection observed in the stratum lacunosum-moleculare confirms *ex vivo* dissection work on human specimens (Yasutaka et al. 2013).

Beyond this portion of the perforant path system, the contrast and resolution of this technique provides further information on the remainder of anatomy and circuitry of the MTL. The remarkably consistent conspicuity of the inner one-third of the dentate molecular layer containing fibers tangential with the granular cell layer, and the almost mirror-like appearance of the adjacent polymorphic layer, raises the importance of the mossy cell dentate pathway. Mossy cells (unrelated to mossy fibers) of the polymorphic layer are known to produce projections to the ipsilateral (associational, found in rat, monkey, and human) and contralateral (commissural, only found in the rat) inner one-third of the dentate gyrus (Amaral et al. 1984; Seress and Ribak 1984; Demeter et al. 1985; Ribak et al. 1985; Frotscher et al. 1991). Given this literature and the limited evidence in humans confirming the lack of hippocampal commissural fibers (Wilson et al. 1991), this finding we are visualizing throughout the dentate likely reflects the associational mossy cell pathway constituting extensive interconnections with the dentate gyrus.

The principal dentate output via mossy fibers to CA3 and CA4 is unmyelinated, but PLI is primarily sensitive to myelinated axons because of the birefringent property of myelin. Nevertheless, this pathway, which shows a lack of intensity on the transmittance images together with black coloration in the fiber orientation images, can be identified as being mossy fibers, because its position and extent correspond to those of high kainate receptor density. Kainate receptors in the hippocampus have been shown to occur at very high density nearly exclusively in the termination fields of the mossy fibers (Zilles et al. 2002; Zilles and Amunts 2009).

The endfolial pathway was previously thought to be a human-only pyramidal cell output from CA4 (Parekh et al. 2015). It extends superiorly from the hilus into the stratum oriens, synapsing along the way in CA3, and its termination was previously undetermined, but suggested to connect to the Schaffer system (Lim, Mufson, et al. 1997). Here, we can clearly see the endfolial pathway running to the Schaffer collaterals, confirming this

proposed affiliation, and supporting the basis of the trisynaptic model of hippocampal connectivity. The identification of a smaller version of this same pathway in the vervet monkey suggests that this pathway is not unique to humans, but larger when compared with that of the vervet monkey.

PLI is associated with some methodological challenges as follows: It is difficult to determine fiber tracts running perpendicular to the plane of sectioning, because such fiber tracts appear black in fiber orientation images based on polarized light microscopy. To compensate for this, we sectioned, in addition to the 2 human lobes processed in the coronal plane, a third human lobe in the sagittal plane. This enabled us to confirm suspected longitudinal pathways because they are running in-plane over a much longer extent in the sagittal sections. A further challenge of PLI studies is to precisely align the serial sections at high resolution to produce three-dimensional reconstructions of the human brain in order to implement fiber-tracking procedures. This requires supercomputing facilities given the extremely large image sizes and is the object of current efforts. While current implementations of PLI focus on the strong birefringence associated with myelin, unmyelinated axons are also birefringent, though to a much lesser degree. Future work analyzing this lower order birefringence could clearly complement the present results. The spatial orientations of fibers in PLI are based on birefringence measurements of unstained histological sections using a voxel-based analysis with a pixel size in the present study of  $1.3 \times 1.3 \times 70 \mu\text{m}$ . Since single fibers often have a diameter below  $1 \mu\text{m}$ , a fiber orientation vector of each voxel reflects the net effect of all comprised single fibers. Therefore, partial volume effects cannot be completely ignored. However, in most cases, PLI images clearly show the crossing and bending of very small fiber bundles that have diameters well above  $1.3 \mu\text{m}$ , enabling us to resolve crossing fibers in the parahippocampal gyrus. Furthermore, novel methods are under development to compensate for the remaining resolution and partial volume effects (Dohmen et al. 2015; Reckfort et al. 2015). Finally, the 2 humans whose brains were used in this study had diabetes, which can affect microstructure through microvascular ischemia and obscure the visualization of certain tracks though there is not a known predisposition to affect the hippocampus (Biessels and Reijmer 2014; Wisse et al. 2014). Future studies on a greater number of specimens with and without diabetes should confirm the consistency of the findings we observed here.

In conclusion, polarized light microscopy offers hitherto unprecedented direct visualization of the course of myelinated pathways in the human brain without modeling as necessary for DTI analysis and fiber tracking. Evaluation of the human temporal lobe has confirmed pathways based on the animal literature and revealed important differences between animal and human connectivity. Future applications of PLI may more fully discern the circuitry underlying brain function and serve as an anatomic evaluation of DTI data, and a platform to understand mesial temporal diseases.

## Supplementary Material

Supplementary material can be found at: <http://www.cercor.oxfordjournals.org/>.

## Funding

Funding was provided for this study by a Burroughs Wellcome Fund 2013 Collaborative Research Travel Grant to M.M.Z, as well as by the European Union Seventh Framework Programme

(FP7/2007-2013) under grant agreement no. 604102 (Human Brain Project), and the Portfolio Theme “Supercomputing and Modeling for the Human Brain” of the Helmholtz Association, Germany (to K.A. and K.Z.). The work on the vervet brain was supported partly by a National Institutes of Health grant (R01 MH092311).

## Notes

*Conflict of Interest:* M.M.Z. receives research funding from GE Healthcare that is unrelated to polarized light microscopy.

## References

- Amaral DG, Insausti R, Cowan WM. 1984. The commissural connections of the monkey hippocampal formation. *J Comp Neurol*. 224:307–336.
- Amaral DG, Scharfman HE, Lavenex P. 2007. The dentate gyrus: fundamental neuroanatomical organization (dentate gyrus for dummies). *Prog Brain Res*. 163:3–22.
- Andersen P. 2007. *The hippocampus book*. Oxford, New York: Oxford University Press.
- Augustinack JC, Helmer K, Huber KE, Kakunoori S, Zöllei L, Fischl B. 2010. Direct visualization of the perforant pathway in the human brain with ex vivo diffusion tensor imaging. *Front Hum Neurosci*. 4:42.
- Axer M, Amunts K, Gräßel D, Palm C, Dammers J, Axer H, Pietrzyk U, Zilles K. 2011. A novel approach to the human connectome: ultra-high resolution mapping of fiber tracts in the brain. *Neuroimage*. 54:1091–1101.
- Axer M, Gräßel D, Kleiner M, Dammers J, Dickscheid T, Reckfort J, Hutz T, Eiben B, Pietrzyk U, Zilles K, et al. 2011. High-resolution fiber tract reconstruction in the human brain by means of three-dimensional polarized light imaging. *Front Neuroinformatics*. 5:34.
- Biessels GJ, Reijmer YD. 2014. Brain changes underlying cognitive dysfunction in diabetes: what can we learn from MRI? *Diabetes*. 63:2244–2252.
- Braak H. 1980. *Architectonics of the human telencephalic cortex*. Berlin, New York: Springer.
- Chrobak JJ, Amaral DG. 2007. Entorhinal cortex of the monkey: VII. Intrinsic connections. *J Comp Neurol*. 500:612–633.
- Demeter S, Rosene DL, Van Hoesen GW. 1985. Interhemispheric pathways of the hippocampal formation, presubiculum, and entorhinal and posterior parahippocampal cortices in the rhesus monkey: the structure and organization of the hippocampal commissures. *J Comp Neurol*. 233:30–47.
- Ding SL. 2013. Comparative anatomy of the prosubiculum, subiculum, presubiculum, postsubiculum, and parasubiculum in human, monkey, and rodent. *J Comp Neurol*. 521:4145–4162.
- Ding SL, Van Hoesen GW. 2015. Organization and detailed parcellation of human hippocampal head and body regions based on a combined analysis of cyto- and chemoarchitecture. *J Comp Neurol*. 523:2233–2253.
- Dohmen M, Menzel M, Wiese H, Reckfort J, Hanke F, Pietrzyk U, Zilles K, Amunts K, Axer M. 2015. Understanding fiber mixture by simulation in 3D polarized light imaging. *Neuroimage*. 111:464–475.
- Fiala M. 2005. ARTag, a fiducial marker system using digital techniques. In: *Computer vision and pattern recognition*. CVPR 2005. IEEE Computer Society Conference on. p. 590–596.

- Frotscher M, Seress L, Schwerdtfeger WK, Buhl E. 1991. The mossy cells of the fascia dentata: a comparative study of their fine structure and synaptic connections in rodents and primates. *J Comp Neurol.* 312:145–163.
- Gómez-Isla T, Price JL, McKeel DW Jr, Morris JC, Growdon JH, Hyman BT. 1996. Profound loss of layer II entorhinal cortex neurons occurs in very mild Alzheimer's disease. *J Neurosci.* 16:4491–4500.
- Hamlyn LH. 1962. The fine structure of the mossy fibre endings in the hippocampus of the rabbit. *J Anat.* 96:112–120.
- Heinsen H, Gossmann E, Rub U, Eisenmenger W, Bauer M, Ulmar G, Bethke B, Schuler M, Schmitt HP, Gotz M, et al. 1996. Variability in the human entorhinal region may confound neuropsychiatric diagnoses. *Acta Anat (Basel).* 157:226–237.
- Hevner RF, Kinney HC. 1996. Reciprocal entorhinal-hippocampal connections established by human fetal midgestation. *J Comp Neurol.* 372:384–394.
- Insausti R, Amaral DG. 2004. Hippocampal formation. In: Paxinos G, Mai JK, editors. *The human nervous system*, 2nd ed. London: Academic Press. p. 871–914.
- Insausti R, Juottonen K, Soininen H, Insausti AM, Partanen K, Vainio P, Laakso MP, Pitkänen A. 1998. MR volumetric analysis of the human entorhinal, perirhinal, and temporopolar cortices. *AJNR Am J Neuroradiol.* 19:659–671.
- Insausti R, Tunon T, Sobreviela T, Insausti AM, Gonzalo LM. 1995. The human entorhinal cortex: a cytoarchitectonic analysis. *J Comp Neurol.* 355:171–198.
- Jenkinson M, Beckmann CF, Behrens TE, Woolrich MW, Smith SM. 2012. *Fsl. Neuroimage.* 62:782–790.
- Kalus P, Slotboom J, Gallinat J, Mahlberg R, Cattapan-Ludewig K, Wiest R, Nyffeler T, Buri C, Federspiel A, Kunz D, et al. 2006. Examining the gateway to the limbic system with diffusion tensor imaging: the perforant pathway in dementia. *Neuroimage.* 30:713–720.
- Kerchner GA, Deutsch GK, Zeineh M, Dougherty RF, Saranathan M, Rutt BK. 2012. Hippocampal CA1 apical neuropil atrophy and memory performance in Alzheimer's disease. *Neuroimage.* 63:194–202.
- Kondo H, Lavenex P, Amaral DG. 2008. Intrinsic connections of the macaque monkey hippocampal formation: I. Dentate gyrus. *J Comp Neurol.* 511:497–520.
- Kondo H, Lavenex P, Amaral DG. 2009. Intrinsic connections of the macaque monkey hippocampal formation: II. CA3 connections. *J Comp Neurol.* 515:349–377.
- Kress GJ, Dowling MJ, Meeks JP, Mennerick S. 2008. High threshold, proximal initiation, and slow conduction velocity of action potentials in dentate granule neuron mossy fibers. *J Neurophysiol.* 100:281–291.
- Lim C, Blume HW, Madsen JR, Saper CB. 1997. Connections of the hippocampal formation in humans: I. The mossy fiber pathway. *J Comp Neurol.* 385:325–351.
- Lim C, Mufson EJ, Kordower JH, Blume HW, Madsen JR, Saper CB. 1997. Connections of the hippocampal formation in humans: II. The endfolial fiber pathway. *J Comp Neurol.* 385:352–371.
- Mueller SG, Weiner MW. 2009. Selective effect of age, Apo e4, and Alzheimer's disease on hippocampal subfields. *Hippocampus.* 19:558–564.
- Parekh MB, Rutt BK, Purcell R, Chen Y, Zeineh MM. 2015. Ultra-high resolution in-vivo 7.0T structural imaging of the human hippocampus reveals the endfolial pathway. *Neuroimage.* 112:1–6.
- Reckfort J, Wiese H, Pietrzyk U, Zilles K, Amunts K, Axer M. 2015. A multiscale approach for the reconstruction of the fiber architecture of the human brain based on 3D-PLI. *Front Neuroanat.* 9:118.
- Ribak CE, Seress L, Amaral DG. 1985. The development, ultra-structure and synaptic connections of the mossy cells of the dentate gyrus. *J Neurocytol.* 14:835–857.
- Rosene D, Van Hoesen G. 1987. The hippocampal formation of the primate brain. A review of some comparative aspects of cytoarchitecture and connections. In: Jones EG, Peters A, editors. *Cerebral Cortex*, Vol. 6. New York: Plenum Press. p. 345–456.
- Rosene DL, Van Hoesen GW. 1977. Hippocampal efferents reach widespread areas of cerebral cortex and amygdala in the rhesus monkey. *Science.* 198:315–317.
- Saunders RC, Aggleton JP. 2007. Origin and topography of fibers contributing to the fornix in macaque monkeys. *Hippocampus.* 17:396–411.
- Saunders RC, Rosene DL. 1988. A comparison of the efferents of the amygdala and the hippocampal formation in the rhesus monkey: I. Convergence in the entorhinal, prorrhinal, and perirhinal cortices. *J Comp Neurol.* 271:153–184.
- Seress L, Ribak CE. 1984. Direct commissural connections to the basket cells of the hippocampal dentate gyrus: anatomical evidence for feed-forward inhibition. *J Neurocytol.* 13:215–225.
- Stephan H. 1975. *Alloccortex*. Berlin, Heidelberg, New York: Springer.
- Suzuki WA, Amaral DG. 1994. Topographic organization of the reciprocal connections between the monkey entorhinal cortex and the perirhinal and parahippocampal cortices. *J Neurosci.* 14:1856–1877.
- Tournier J-D, Yeh C-H, Calamante F, Cho K-H, Connolly A, Lin C-P. 2008. Resolving crossing fibres using constrained spherical deconvolution: validation using diffusion-weighted imaging phantom data. *Neuroimage.* 42:617–625.
- Wagner D, Schmalstieg D. 2007. ARTToolKitPlus for pose tracking on mobile devices. In: *12th Computer Vision Winter Workshop*. p. 139–146.
- Wilson CL, Isokawa M, Babb TL, Crandall PH, Levesque MF, Engel J Jr. 1991. Functional connections in the human temporal lobe. II. Evidence for a loss of functional linkage between contralateral limbic structures. *Exp Brain Res.* 85:174–187.
- Wisse LE, de Bresser J, Geerlings MI, Reijmer YD, Portegies ML, Brundel M, Kappelle LJ, van der Graaf Y, Biessels GJ, Utrecht Diabetic Encephalopathy Study Group, SMART-MR Study Group. 2014. Global brain atrophy but not hippocampal atrophy is related to type 2 diabetes. *J Neurol Sci.* 344:32–36.
- Witter MP, Amaral DG. 1991. Entorhinal cortex of the monkey: V. Projections to the dentate gyrus, hippocampus, and subicular complex. *J Comp Neurol.* 307:437–459.
- Yassa MA, Muftuler LT, Stark CE. 2010. Ultrahigh-resolution microstructural diffusion tensor imaging reveals perforant path degradation in aged humans in vivo. *Proc Natl Acad Sci USA.* 107:12687–12691.
- Yasutaka S, Shinohara H, Kominami R. 2013. Gross anatomical tractography (GAT) proposed a change from the “Two laminae concept” to the “Neuronal unit concept” on the structure of the human hippocampus. *Okajimas Folia Anat Jpn.* 89:147–156.
- Zeineh MM, Engel SA, Thompson PM, Bookheimer SY. 2003. Dynamics of the hippocampus during encoding and retrieval of face-name pairs. *Science.* 299:577–580.
- Zeineh MM, Holdsworth S, Skare S, Atlas SW, Bammer R. 2012. Ultra-high resolution diffusion tensor imaging of the

microscopic pathways of the medial temporal lobe. *Neuroimage*. 62:2065–2082.

Zeineh MM, Parekh MB, Zaharchuk G, Su JH, Rosenberg J, Fischbein NJ, Rutt BK. 2014. Ultrahigh-resolution imaging of the human brain with phase-cycled balanced steady-state free precession at 7T. *Invest Radiol*. 49:278–289.

Zilles K, Amunts K. 2009. Receptor mapping: architecture of the human cerebral cortex. *Curr Opin Neurol*. 22:331–339.

Zilles K, Schleicher A, Palomero-Gallagher N, Amunts K. 2002. Quantitative analysis of cyto- and receptor architecture of the human brain. In: Toga AW, Mazziotta JC, editors. *Brain mapping: the methods*, 2nd ed. San Diego, CA: Academic Press. p. 573–602.